BNL-224405-2023-JAAM

Operando characterization and regulation of metal dissolution and redeposition dynamics near battery electrode surface

Y. Zhang, S. Hwang

To be published in "Nature Nanotechnology"

April 2023

Center for Functional Nanomaterials

Brookhaven National Laboratory

U.S. Department of Energy

USDOE Office of Science (SC), Basic Energy Sciences (BES) (SC-22)

DISCLAIMER

Operando Characterization and Regulation of Metal Dissolution and Redeposition Dynamics near Battery Electrode Surface

Yuxin Zhang[1], Anyang Hu[1], Dawei Xia[1], Sooyeon Hwang[2*], Sami Sainio[3], Dennis Nordlund[3], F. Marc Michel[4], Robert B. Moore[1,5], Luxi Li[6*], Feng Lin[1,5,7*]

1 Department of Chemistry, Virginia Tech, Blacksburg, VA 24073, USA

2 Center for Functional Nanomaterials, Brookhaven National Laboratory, Upton, NY 11973, USA

3 Stanford Synchrotron Radiation Lightsource, SLAC National Accelerator Laboratory, Menlo Park, CA 94025, USA

4 Department of Geosciences, Virginia Tech, Blacksburg, VA 24061, USA.

5 Macromolecules Innovation Institute, Virginia Tech, Blacksburg, VA 24061, USA

6 Advanced Photon Source, Argonne National Laboratory, Lemont, IL 60439, USA

7 Department of Materials Science and Engineering, Virginia Tech, Blacksburg, VA 24061, USA

*E-mail: fenglin@vt.edu, luxili@anl.gov, soohwang@bnl.gov

ORCID numbers

Feng Lin: 0000-0002-3729-3148

Luxi Li: 0000-0002-9259-8796

Sooyeon Hwang: 0000-0001-5606-6728

Abstract

Mn dissolution has been a longstanding, ubiquitous issue that negatively impacts the performance of Mn-based battery materials. Mn dissolution involves complex chemical and structural transformations at the electrode-electrolyte interface. The continuously evolving electrode-electrolyte interface has posed great challenges for characterizing the dynamic interfacial process and quantitatively establishing the correlation with battery performance. In this study, we visualize and quantify the temporally and spatially resolved Mn dissolution/redeposition (D/R) dynamics of electrochemically operating Mn-containing cathodes. The particle-level and electrode-level analyses reveal that the D/R dynamics is associated with distinct interfacial degradation mechanisms at different states of charge. Our results statistically differentiate the contributions of surface reconstruction and Jahn-Teller distortion to the Mn dissolution at different operating voltages. Introducing sulfonated polymers (Nafion) into composite electrodes can modulate the D/R dynamics through trapping the dissolved Mn species and rapidly establishing the local Mn D/R equilibrium. This work represents an inaugural effort to pinpoint the chemical and structural transformations responsible for Mn dissolution via an *operando* synchrotron study and develops an effective method to regulate Mn interfacial dynamics for improving battery performance.

Main

Mn-containing battery materials can increase sustainability and reduce the cost of mass-produced rechargeable batteries[1–6]. However, most of these materials can undergo degradation due to the interplay between the Jahn-Teller distortion active Mn species and irreversible structural changes during battery operation[7–11]. Many of the degradation processes originate at the electrochemical interface and are interconnected at the nanometric scale[12–15]. Understanding the relationships between different interfacial processes (i.e., particle-to-particle, particle-to-electrolyte) has been a longstanding challenge for the battery community. In commercial non-aqueous Li-ion batteries, the high vapor pressure of non-aqueous solvents and the air-sensitive salt prohibit the observation of interfacial evolution under operating conditions. As such, most previous studies utilized *ex situ* characterizations to probe the electrode surface after cycling[9,16–18], lacking temporal resolution. Furthermore, *in situ* techniques such as transmission electron microscopy show excellent temporal and spatial resolution but typically lack the statistical specificity for the complex and heterogeneous electrode surface[19,20]. Thus, the particle and electrode heterogeneities were rarely considered, albeit their significance in degradation mechanism and battery performance. Therefore, a multidimensional *operando* investigation of Mn-based cathode is urgently needed to statistically elucidate the dynamics of cathode surface and degradation mechanisms with temporal and spatial resolution.

Spinel $LiMn_2O_4$ (LMO) represents one of the most classical Mn-based cathodes in rechargeable Li-ion batteries[21–24]. During battery cycling, the electrochemical interface deviates from the equilibrium, resulting in various interfacial degradations. It is widely argued that driven by the Mn^{3+} Jahn-Teller (J-T) distortion and $2Mn^{3+} \rightarrow Mn^{2+} + Mn^{4+}$ disproportionation, LMO suffers from pronounced Mn dissolution accelerated by proton at the electrode-electrolyte interface, which

aggravates the electrolyte decomposition and impedance growth on the anode surface[7,16,25]. The dissolution can also be associated with surface reconstruction[18], i.e., formation of Mn_3O_4, layered or rocksalt phases, at high voltages (>4.2 V vs. Li/Li^+)[9,26], However, the interplay between distinct mechanisms remains elusive and calls for a more comprehensive study.

Mn redeposition is another crucial issue that is even more insufficiently investigated. The dissolved metal cations can deposit onto the electrode surface under the electric field[8,27]. The ion speciation across the electrochemical interface, especially metal dissolution/redeposition (D/R) dynamics, will further modify the chemistry and structure of electrode surfaces, giving rise to varied cell performance and making the surface analysis highly challenging[8,27–31]. Tracking D/R dynamics at the electrode level can reveal the metal dissolution mechanism and quantitatively correlate the Mn loss with performance decay. Although the influences of dissolved Mn on the properties of battery components (i.e., cathode, anode, electrolyte) have attracted extensive research attention[25,27,32], the metal D/R dynamics and mechanisms at different states of charge (SOCs) are poorly understood because reactions are spatially confined at the electrochemical interface and dynamically evolve, imposing challenges for experimental measurements.

The regulation and suppression of Mn dissolution constitutes an important factor in practical applications of Mn-based cathodes. Trapping the dissolved Mn species through coating to manipulate the Mn D/R dynamics is a promising direction while lacking exploration. Considering that the sulfonate groups in polymer can coordinate with transition metal cations and affect the transport kinetics of different ions[33,34], introducing foreign polymer additives into the Mn-based cathodes is a potential approach to effectively inhibiting Mn dissolution.

Since LMO has decent structural integrity in neutral water at the pristine state, the LMO-based electrode operated in the dilute aqueous electrolyte offers a desirable platform for the *operando*

observation of Mn D/R dynamics. Therefore, in this work, we report the real-time visualization and quantification of the D/R dynamics with single-particle resolution and electrode-scale statistical analyses. We reveal the SOC-dependent Mn dissolution mechanisms of LMO cycled in the aqueous electrolyte. The J-T distortion is the root cause for Mn dissolution at low SOCs (< 1.0 V vs. Ag/AgCl). When the voltage is higher than 1.0 V vs Ag/AgCl, surface reconstruction and J-T distortion coexist and impose different effects on Mn dissolution. Specifically, the surface reconstruction-induced Mn dissolution dominates the medium voltage range (1.0 – 1.2 V vs. Ag/AgCl), and the J-T distortion-induced Mn dissolution governs the high voltage range (1.2 – 1.55 V vs. Ag/AgCl). Sulfonated tetrafluoroethylene (i.e., Nafion), present at the surface of active particles, coordinates strongly with dissolved Mn cations, reduces proton conductivity, and improves cell kinetics and cycle life. The present study creates insights into manipulating Mn D/R dynamics at the electrochemical interface for rechargeable batteries.

Dynamic Mn D/R behaviors during the Electrochemical Cycling

We choose a 2 M lithium bis(trifluoromethanesulfonyl)imide (LiTFSI) aqueous electrolyte to investigate the Mn D/R dynamics in the LMO electrode. Such a dilute electrolyte can accelerate Mn dissolution to a quantifiable concentration within a short cycling period, allowing for *in situ* and *operando* studies. **Figure 1a** shows the cyclic voltammetry (CV) of the phase pure LMO (**Figure S1**), with a pair of oxidation/reduction peaks corresponding to the Mn^{3+}/Mn^{4+} redox couple. The high current density near the upper cutoff voltage is contributed collectively by the Mn oxidation reaction and oxygen evolution reaction (OER). The materials degradation can be observed by the gradual peak current decay within 15 cycles. We then applied the *in situ* X-ray fluorescence microscopy (XFM) method[35] to track Mn distribution at the electrode level throughout electrochemical cycling (**Extended Data Figure 1**). The pristine drop-casted LMO

electrode shows a heterogeneous Mn distribution (**Figure 1b**) with some aggregated regions. Due to Mn dissolution, continuous CV cycling lowers the intensity of the high-concentration regions and reduces the overall heterogeneity of the Mn distribution. We then program the data acquisition time for each XFM map to be identical to the time needed for each CV cycle, which allows us to track the net Mn concentration change following each cycle. We observe that the Mn concentration exhibits a monotonic decrease within the first ten cycles and then becomes stabilized in the following cycles (**Figure 1c**). The net concentration change presented here reflects that the Mn D/R process favors dissolution until an equilibrium is reached after 10 CV cycles.

We subsequently program the data acquisition time for each XFM map to be longer than the time needed for each CV cycle, which allows each XFM map to cover more than one complete CV cycle. The Mn concentration exhibits non-monotonic fluctuations (**Figure 1d**), which suggests the voltage-dependent D/R behaviors. Indeed, when we perform chronoamperometry (CA) measurements at different potentials, the Mn concentration decreases at the positive potential (0.9 V) and increases at the negative potential (-0.1 V, **Figures S2** and **S3**).

We further conduct pixel-by-pixel mathematical subtractions between neighboring maps (**Figure S4**) to obtain spatially resolved Mn concentration changes between adjacent CV cycles. The negative and positive concentration changes correspond to Mn net concentration loss (dissolution > redeposition) and net concentration gain (redeposition > dissolution) between neighboring maps, respectively (**Figure 1e**). The subtraction between the 2^{nd} and 3^{rd} cycles yields a broader and more negatively shifted histogram, indicating that the Mn D/R is more heterogeneous and there is a net Mn concentration loss during the early cycles. In contrast, the subtraction between the 14^{th} and 15^{th} cycle yields a narrower histogram centered at 0% relative concentration change. The comparison between the two subtractions further demonstrates a more pronounced dissolution

behavior during early cycles, consistent with **Figure 1c**. Since LMO particles are susceptible to the dissolution and redeposition once they are electrochemically cycled, we conjecture the pixels that experience 0% relative concentration change are electrochemically inactive LMO domains. As shown in **Figure S5**, the inactive domains expand significantly after the 8th cycle. Noted that the value could be overestimated owing to the possibility that a small fraction of active LMO particles may remain stable with no Mn dissolution during electrochemical cycling. In summary, the D/R dynamics decreases the redox-active Mn species and increases the population of inactive LMO domains, contributing to the performance decay. The distinct D/R dynamics during the CV cycling, especially the non-monotonicity, motivates us to investigate the voltage-dependent D/R dynamics.

Voltage-dependent Mn D/R Dynamics

LMO shows noticeable capacity decay when cycled in the 2 M LiTFSI aqueous electrolyte using the constant current charging-discharging method (**Figure 2a**). We then investigate the voltage-dependent Mn dissolution with single-particle resolution during the first charging process (**Figure 2b**). The Mn concentration gradually decreases during charging, accompanied by the dramatic particle shrinkage above 1.0 V. The quantitative analysis (**Figure 2c**) and corresponding first derivatives of the curve (**Figure S6**) reveal that the Mn concentration exhibits more severe loss when the voltage is higher than 1.0 V. The data point at ~1700 s in **Figure S6** deviates from the neighboring points and could origin from the systematic error (i.e., signal fluctuation). The apparent Mn dissolution rate is facilitated between 1.0 – 1.2 V and gets more facilitated when holding at 1.2 V. More detailed analyses of different particles reveal that the Mn concentration variation ranges from -60% to +4% at the single-particle level (**Extended Data Figure 2**), which could be impacted by the position of the particles in the electrode and the interaction with the

neighboring particles. Therefore, an electrode-level analysis with ensemble-averaged information from many particles can represent the overall Mn D/R behaviors during cycling.

At the electrode level, we further divide the *in situ* first charging profile into low voltage range 0.3 – 1 V), medium voltage range (MV, 1.0 – 1.2 V), and high voltage range (HV, 1.2 V – 1.55 V) (**Figure 2d**). The charging capacity at LV and MV is contributed by Mn oxidation, and the capacity at HV is attributed to the oxygen evolution reaction (OER). From **Figure 2e** we can observe that, compared to the sluggish Mn loss at the LV range, rapid Mn dissolution takes place at the MV and beginning of HV ranges. Moreover, during the holding process at 1.2 V**,** we can notice that the Mn concentration experiences a severe drop at the initial stage (**Figure 2e**), in line with the feature we observed at the single-particle level (**Figure 2c**) and corresponding to high dissolution rate, and it gets stabilized upon elongated voltage holding at 1.2 V, suggesting a dynamic equilibrium of dissolution and redeposition processes. The accumulated Mn loss is 3.0%, 3.8%, and 3.2% at LV, MV, and HV, respectively, which shows that the medium-voltage charging, albeit providing only 21 mA/g capacity (23% of the total charge capacity), introduces the most severe Mn dissolution. The Mn D/R behaviors in the following charging processes exhibit a non-monotonic feature and becomes more complicated (**Figure S7**), which could be attributed to the further interaction between electrode particles and gradually accumulated Mn species at the electrode-electrolyte interface. The overall Mn loss shows large discrepancy between the single-particle and electrode-scale measurements. Between OCV and 1.2 V, the single-particle measurement has a 40.4% loss, while the electrode-scale measurement has a 6.8% loss. Some particles experience higher degrees of redox reactions and therefore a more severe Mn dissolution behavior than other particles, indicating a heterogeneous charge distribution at the electrode level[36,37]. Moreover, at both MV and HV ranges, we observe a Gaussian-like distribution in the

pixel-by-pixel analyses of the Mn D/R dynamics (**Figure 2f**), which suggests that both Mn dissolution and redeposition take place when the LMO undergoes charging. Meanwhile, by using the graphite paper as the counter electrode, we show that the dissolved species can not only redeposit on the LMO surface but also migrate through the electrolyte and deposit on the counter electrode (**Extended Data Figure 3**). Overall, our results show a voltage-dependent, continuously evolved Mn D/R behavior upon constant current charging.

Voltage-Dependent Structural and Chemical Transformations

To shed light on the Mn dissolution mechanism at different voltage ranges, we apply *in situ* hard X-ray absorption spectroscopy (XAS) to investigate the bulk properties of LMO upon cycling. We select five states-of-charge (SOCs), i.e., the pristine, 1.0 V, 1.2 V, 1.45 V, and discharged states (**Figure 3a**). Based on the whiteline energy of references and LMO samples, we show that Mn is continuously oxidized from 3.5+ at the pristine state to 3.9+ at 1.2 V charged state while demonstrate negligible change at the HV region (**Figure 3b-d**). Extended X-ray absorption fine structure (EXAFS, **Figure 3e**) reveals that the Mn-O and Mn-Mn interatomic distances experience abnormal elongation when LMO enters the HV range (**Figure 3f**). The EXAFS fitting results show that the corresponding Mn-O coordination number is reduced from six to five (**Figure 3g**, **Figure S8**, **Figure S9** and **Table S1-5**). These results collectively reveal the structural degradation of LMO induced by the OER at HV, originating from the lattice oxygen loss[32]. Since particle surface can directly interact with the electrolyte, it is expected that the surface will undergo the most pronounced structural change upon cycling, as confirmed by previous studies regarding the surface reconstruction in layered cathode materials[18]. Therefore, understanding the surface structural change is crucial to revealing the LMO degradation mechanism in aqueous electrolytes.

To gain more insights into the surface reconstruction of LMO upon charging, we conduct a suite of surface-sensitive characterizations. The HAADF-STEM images along [110] zone axis of pristine materials confirm a well-defined spinel LMO phase from particle surface to bulk (**Figure S10**). After charging to 1 V, a transition phase between spinel LMO and Mn_3O_4 appears on the surface (**Figure S11**)[9], which is further transformed to pure Mn_3O_4 phase when the electrode is charged to 1.2 V (**Figure S12**). Meanwhile, the intensity of Mn atoms with lower stacking density gets greatly diminished at the surface, and such feature becomes more pronounced in the 1.55 V charged particles (**Figure S13**). The Mn dissolution behavior of Mn_3O_4 (**Extended Data Figure 4**) and MnO_2 (**Extended Data Figure 5**) proves that the Mn loss at 1.2 V mainly originates from Mn_3O_4 dissolution owing to the relatively weak chemical bond between Mn^{2+} and oxygen anions. The Mn $L_{2,3}$ electron energy loss spectra (EELS) of 1.55 V charged LMO particles exhibit blue shift (**Figure 3h** and **3i**) moving from the surface to the bulk, confirming that Mn is reduced on the surface. The thickness of the surface reduction layer is estimated to be ~10 nm, consistent with the thickness of the distorted region in the HAADF-STEM image (**Figure S13**). We believe such a thick surface reconstruction layer is caused by the thermodynamic instability of the delithiated LMO and the electrode-electrolyte side reaction. After 20 cycles, the particle becomes porous with polycrystalline structures and amorphous phases emerging on the surface (**Figure S14**), suggesting a severe distortion of LMO structure in dilute aqueous electrolytes. The soft XAS results show that LMO undergoes a typical oxidation process upon charging to 1 V (**Figure 3j**). However, upon charging to 1.2 V (MV) and 1.55 V (HV), Mn at the surface becomes reduced, in agreement with the EELS results and confirming the emergence of surface reconstruction. The appearance of a mixed states of Mn^{2+} and Mn^{3+} species at MV proves the formation of Mn_3O_4 on the particle surface, which agrees with previous observations in non-aqueous electrolytes[9]. These findings

suggest that a higher degree of structural distortion occurs when voltage is higher than 1 V. Up discharging to 0 V, the surface becomes more oxidized than that at 1.2 V (MV) and 1.55 V (HV), which suggests that the Mn_3O_4 gets dissolved upon discharging, consistent with the hard XAS results in **Figure 3**. Collectively, our results show that there is a correlation between surface reconstruction and Mn dissolution.

Correlations between Mn D/R Dynamics and LMO Transformations

Thus far, our study has found that both D/R dynamics and materials transformation are voltage-dependent. Since the Mn dissolution has been shown to be strongly correlated with materials transformation[7,16], here we statistically establish the correlation between D/R dynamics and materials transformation at different voltage ranges.

The Mn concentration in pristine electrode exhibits non-uniform distribution in the histogram (**Figure S15a**), suggesting the heterogeneous loading of the as-prepared LMO electrode. We divide the initial electrode loading into four categories based on the Mn XFM concentration map, namely, Low C, Medium-Low C, Medium-High C, and High-C. The area under the curve (AUC) in the concentration histogram reflects the total Mn concentration and is used to separate different categories, where each category occupies 25% of AUC (**Figure S15a**). Meanwhile, at each voltage range, we can categorize the D/R dynamics into four scenarios based on the net change of the local Mn concentration, i.e., mild net dissolution, mild net redeposition, severe net dissolution, and severe net redeposition domains (**Figure S15b**). These two categorizations allow us to quantitatively correlate D/R dynamics, initial LMO loading, and voltage range. By comparing the D/R dynamics with the same scenario (i.e., same color-coded data points in **Figure S16**) at different voltage ranges, we observe that the LV and HV ranges display similar characteristics and

are distinct from the MV range (**Figure S16**). Therefore, the driving force behind the D/R dynamics at the LV and HV ranges is distinct from that at the MV range.

Combining with the characterization results (**Figure 3**), we propose the correlation between the D/R dynamics and voltage-dependent materials transformations (**Figure 4**). When LMO is charged from 0.3 V to 1.0 V (LV range), a substantial amount of Mn still remains at the J-T active Mn^{3+} state due to the low charge capacity (low Mn oxidation), leading to noticeable Mn dissolution in the presence of hydronium in the water. When the voltage is between 1.0 to 1.2 V, the delithiated LMO particles undergo surface reconstruction and the emergence of soluble Mn^{2+} in Mn_3O_4 dominates the Mn dissolution behavior. Once the LMO is further charged to the OER potential (i.e., HV range), protons gradually accumulate near the electrode surface due to the decreased OH^- concentration caused by the OER. Since the capacity of LMO is smaller than the theoretical value (148 mAh/g) and our hard XAS results in **Figure 3g** shows that the Mn is not fully oxidized at 1.55 V, there are many particles remain partially charged even at the HV range, indicating heterogeneous charge distribution at the electrode level (particle with different color codes in **Figure 4**), which is associated with the different Mn D/R behaviors at the particle level (**Extended Data Figure 2**). The enriched proton species near the electrode surface aggravates the disproportion of residual Mn^{3+} and makes the J-T distortion-induced Mn dissolution become the primary factor responsible for Mn dissolution. Moreover, the strong acidic environment drastically interferes with the Mn local bonding and induces more lattice oxygen loss compared to the LV range (**Figure 3g**). Therefore, the dissolution rate at HV range is significantly boosted (**Figure 2e**). We believe the Mn D/R dynamics and corresponding degradation mechanisms we present here can also inform insights into the non-aqueous system, where the proton species are generated by the ethylene carbonate and $LiPF_6$ interacting with trace moisture in the electrolytes. Therefore, we

also evaluate the Mn D/R behavior of LMO in organic solvents. Herein, the tetraethylene glycol dimethyl ether (TEG-DME) with a low vapor pressure is selected as the solvent. As shown in **Extended Data Figure 6**, the Mn dissolution is significantly inhibited in the 2 M LiTFSI-TEG-DME electrolytes owing to the reduced proton concentration. The accumulative Mn loss is estimated to be ~1.5% upon the first charging process, and proton generated as a result of ether decomposition is a primary reason that leads to Mn dissolution[38]. Considering that the sealing of our operando cell is less stringent than that of a coin-cell or pouch-cell configuration, and the net Mn dissolution could be overestimated in this case due to the moisture impact.

Regulating Mn D/R Dynamics with Sulfonated Polymers

Our results have revealed that the surface reconstruction at the MV range leads to the most severe Mn dissolution when the upper cutoff voltage is set to 1.2 V vs. Ag/AgCl. Hence, inhibiting surface reconstruction is expected to significantly improve the performance. Nafion, a cation exchange polymer that allows for selective permeation of cations, has been widely utilized as a coating material in fuel cells and catalysts to reduce the undesired interfacial interactions and alleviate the surface degradation[33,34,39,40]. Herein we discover that simply adding Nafion during the electrode preparation can efficiently mitigate the capacity loss of the composite electrode during cycling. As shown in **Figure 5a**, the capacity retention of the Nafion-added LMO is improved. Compared to the pure LMO, the Nafion-added LMO electrode exhibits smaller reaction overpotentials at the LV range and a higher output capacity (**Figure 5b**). The TEM results in **Figure S17** reveal that the Mn_3O_4 phase appear on the particle surface after Nafion coating owing to the acidic environment in the Nafion solution. The Mn^{2+} in Mn_3O_4 can be easily dissolved into the electrolyte at low voltage, therefore giving rise to more Mn loss at the LV range during *in situ* XFM measurements. (**Figure 5c** and **5d**). In contrast, at the MV range (1.0 – 1.2 V), the Nafion layer

can modify the interaction between LMO and aqueous electrolytes and suppress the Mn dissolution. Importantly, the Nafion-added LMO electrode exhibits negligible net Mn loss in the 4th charge. As shown in **Figure 5e**, this phenomenon could be attributed to the fact that the sulfonate groups in Nafion can ionically associate with the positively charged Mn species and reduce the proton hopping sites[41], which effectively diminishes the proton transport and prevents the surface from the attack of protons. Meanwhile, the trapped Mn^{2+} can accumulate near the particle surface, reducing the time needed to reach the D/R equilibrium (i.e., Le Chatelier's principle). These two factors collectively lead to the suppressed Mn loss in the following cycles. To further validate our hypothesis, we soak the casted Nafion membrane into 2 M $MnSO_4$ aqueous solution for one day. The EDS results confirm the significantly increased Mn concentration in the soaked membranes, and the atomic ratio of S: Mn can reach 1.85, suggesting over 50% of sulfate groups coordinate with Mn species (**Extended Data Figure 7**). Therefore, introducing Nafion into the composite electrodes can improve reaction kinetics, regulate Mn dissolution, and significantly mitigate Mn loss. We also want to highlight that controlling the Nafion concentration is crucial in maintaining the LMO structure and improving the performance. Excessive Nafion solution can lead to rapid capacity decay due to the instability of LMO phase in acidic environments (**Figure S18**). In our study, the weight ratio of LMO: Nafion is controlled to be larger than 150. Moreover, using deprotonated Nafion is another strategy to alleviate the LMO structural change during the modification process.

Conclusion

Understanding and controlling the dynamic Mn D/R behaviors in Mn-based cathodes can reveal electrode degradation mechanisms and more importantly inform the development of methods for stabilizing electrode materials. The continuously evolved speciation at the electrochemical

interface makes it challenging to accurately identify the interfacial degradation processes, such as metal dissolution. Using *in situ* XFM and a suite of surface- and bulk-sensitive techniques, we have developed comprehensive understanding about the Mn D/R dynamics and the corresponding LMO degradation mechanism in the aqueous electrolyte. The continuous Mn dissolution and increased inactive LMO domains collectively leads to performance decay upon cycling. The J-T distortion and surface reconstruction are responsible for the voltage-dependent Mn dissolution behavior. The Mn dissolution exhibits a non-linear relationship with the voltage, and a higher rate can be observed when the surface reconstruction takes place. Introducing Nafion into the electrodes can boost reaction kinetics and inhibit the Mn dissolution especially caused by surface reconstruction. Meanwhile, the trapped Mn^{2+} in Nafion can hinder the proton diffusion towards LMO particle surface and accelerate the establishment of Mn D/R equilibrium, thereby improving cycle life in the dilute electrolyte. The present study directly visualizes and quantifies transition metal D/R dynamics and unravels the role of the sulfonated polymer in controlling D/R dynamics and improving battery performance. The *in situ* experimental methods develop here can be broadly applied to investigate other electrochemical systems that involve solid-liquid interfaces.

Acknowledgment:

The work was supported by the National Science Foundation under no. CBET 1912885 (FL). This research used resources of the Advanced Photon Source, a U.S. Department of Energy (DOE) Office of Science User Facility operated for the DOE Office of Science by Argonne National Laboratory under Contract no. DE-AC02-06CH11357. The use of the Stanford Synchrotron Radiation Light source (SSRL), SLAC National Accelerator Laboratory, was supported by the U.S. Department of Energy, Office of Science, Office of Basic Energy Sciences under Contract no. DE-AC02-76SF00515. This research used electron microscopy resources of the Center for Functional Nanomaterials (CFN), which is a U.S. Department of Energy Office of Science User Facility, at Brookhaven National Laboratory under Contract No. DE-SC0012704. Y.Z. and F.L. thank the beamline scientist Dr. Ryan Davis at SSRL for the help with hard XAS measurements.

Author contribution:

F.L. conceived and led the project. F.L. and Y.Z. designed experiments. Y.Z. performed material synthesis, electrochemical tests, synchrotron measurements, and data analysis. A.H. assisted the XFM measurements. D.X. assisted hard XAS measurements. S.S. and D.N. performed soft XAS measurements. S.H. performed TEM measurements and data analysis. M.M. participated in data discussion. R.B.M. participate in experimental design and data discussion. L.L. assisted XFM measurements and participated in the discussion and data analysis. Y.Z. and F.L. wrote the manuscript with inputs from coauthors. All authors approved the final draft of the manuscript.

Conflict of interest:

The authors declare no conflict of interest.

Figure Legends/Captions:

Figure 1 The dynamic Mn D/R process during the CV cycling in the three-electrode configuration (a) CV profiles of the LMO electrode cycled in a 2 M LiTFSI aqueous electrolyte, where the scan voltage is -0.1 – 1.5 V vs. Ag/AgCl and the scan rate is 5 mV/s; (b) *in situ* XFM mapping of the LMO electrode during the CV cycling, where the color code denotes the relative Mn concentration. The pixel size is 2 μm × 2 μm and the maps are acquired from the 1^{st}, 4^{th}, 7^{th} and 10^{th} cycle, respectively; (c) The relative Mn concentration change calculated from each XFM scan when the time required for each XFM scan (8 min 10 s) is identical to the time per CV cycle (8 min 10 s, 6.5 mV/s), showing continuous Mn dissolution until stabilization after 10 cycles; (d) The relative Mn concentration change calculated from each XFM scan when the time required for each XFM scan (14 min 10 s) is longer than the time per CV cycle (10 min 40 s, 5 mV/s), showing non-monotonic Mn concentration changes; (e) Distribution of relative Mn concentration variation at the beginning and final stages of CV cycling in (c) through pixel-by-pixel analyses. The histogram is obtained by subtracting the corresponding pixel values between two neighboring CV cycles, where a negative value represents Mn dissolution is more than redeposition and a positive value represents Mn redeposition is more than dissolution.

Figure 2 Voltage-dependent Mn dissolution behaviors (a) Charge-discharge profiles of the LMO electrode in the 2 M LiTFSI aqueous electrolyte, where the voltage range is 0 – 1.2 V vs. Ag/AgCl and the current density is 1 C (100 mA/g); (b) The first charging profile (~0.8 C) of *in situ* XFM measurements and the corresponding particle-level Mn concentration maps at different charging voltages. The pixel size is 300 nm × 300 nm and the image size is 12 μm × 15 μm; (c) The particle-level Mn loss ratio calculated from the results in (b); (d) The first charging profile (~0.8 C) of *in situ* XFM measurements for electrode-level analyses, where the voltage was kept constant at 1.2 V and 1.55 V for additional XFM measurements. The blue, yellow, and pink background colors represent low, medium and high voltage ranges, respectively; (e) The electrode-level Mn loss ratio during charging. The voltage holding processes start from the data points labeled with 1.2 V and 1.55 V; (f) Pixel-by-pixel analyses of the Mn D/R dynamics at the MV and HV ranges.

Figure 3 Chemical and structural transformation of LMO during electrochemical cycling (a) Charge-discharge profile of in-situ hard XAS measurements, where the current density is 0.2 C (20 mA/g); (b) Mn K-edge hard XAS spectra at different states of charge (SOCs) and (c) the corresponding Zoom-in of the whiteline region; (d) The whiteline energy as a function of SOCs; (e) Fourier-transformed magnitude of Mn K-edge EXAFS at different SOCs; (f) Inter-atomic distance at different SOCs; (g) Coordination numbers for Mn-O and Mn-Mn obtained from Mn K-edge EXAFS simulations. The error bars are generated on the basis of the EXAFS simulation errors. (h) HAADF-STEM image for the scanning pathway; (i) Mn $L_{2,3}$-edge EELS spectra along the scanning pathway; (j) Mn L_3-edge soft XAS spectra of LMO electrodes at different SOCs. The measurements were conducted using the surface sensitive TEY mode.

Figure 4 Mn dissolution mechanism of LMO in aqueous electrolytes Scheme of the voltage-dependent Mn dissolution mechanisms, where the asterisk symbol indicates the primary degradation driving forces. The different colors of LMO particles indicate different SOCs, where the red color suggests highest SOC while the white color suggests lowest SOC. The particles close to current collector exhibits higher SOC compared to the particles far from the current collector. The yellow arrow indicates the change of bond length. The OCV stands for open circuit voltage.

Figure 5 The electrochemical performance and underlying Mn dissolution behavior of Nafion-added LMO materials (a) Charge-discharge profiles of Nafion-added LMO electrodes in the 2 M LiTFSI aqueous electrolyte, where the voltage range is 0 – 1.2 V vs. Ag/AgCl and the current density is 1 C (100 mA/g); (b) The comparison of the first charging curve of pure LMO and Nafion-added LMO, where the Nafion-added LMO shows smaller overpotentials upon charging; (c) *in situ* XFM mapping of the Nafion added LMO at different state of charge, where the color code denotes the Mn concentration. The pixel size is 2 μm × 2 μm and image size is 100 μm × 100 μm; (d) the Mn loss of pure LMO and Nafion-added LMO electrodes upon charging; (e) the scheme of chemical environment surrounding Nafion-added LMO particles during the fourth charging process.

References:

(1) Thackeray, M. M.; Amine, K. $LiMn_2O_4$ Spinel and Substituted Cathodes. *Nat. Energy* **2021**, *6* (5), 566.

(2) Kim, D. K.; Muralidharan, P.; Lee, H.-W.; Ruffo, R.; Yang, Y.; Chan, C. K.; Peng, H.; Huggins, R. A.; Cui, Y. Spinel $LiMn_2O_4$ Nanorods as Lithium Ion Battery Cathodes. *Nano Lett.* **2008**, *8* (11), 3948–3952.

(3) Xia, H.; Luo, Z.; Xie, J. Nanostructured $LiMn_2O_4$ and Their Composites as High-Performance Cathodes for Lithium-Ion Batteries. *Prog. Nat. Sci. Mater. Int.* **2012**, *22* (6), 572–584.

(4) Lun, Z.; Ouyang, B.; Cai, Z.; Clément, R. J.; Kwon, D.-H.; Huang, J.; Papp, J. K.; Balasubramanian, M.; Tian, Y.; McCloskey, B. D. Design Principles for High-Capacity Mn-Based Cation-Disordered Rocksalt Cathodes. *Chem* **2020**, *6* (1), 153–168.

(5) Li, H.; Fong, R.; Woo, M.; Ahmed, H.; Seo, D.-H.; Malik, R.; Lee, J. Toward High-Energy Mn-Based Disordered-Rocksalt Li-Ion Cathodes. *Joule* **2022**, 6(1), 53–91.

(6) Zhang, Y.; Hu, A.; Liu, J.; Xu, Z.; Mu, L.; Sainio, S.; Nordlund, D.; Li, L.; Sun, C.; Xiao, X. Investigating Particle Size-Dependent Redox Kinetics and Charge Distribution in Disordered Rocksalt Cathodes. *Adv. Funct. Mater.* **2022**, *32* (17), 2110502.

(7) Sun, X.; Xiao, R.; Yu, X.; Li, H. First-Principles Simulations for the Surface Evolution and Mn Dissolution in the Fully Delithiated Spinel LiMn2O4. *Langmuir* **2021**, *37* (17), 5252–5259.

(8) Zhan, C.; Wu, T.; Lu, J.; Amine, K. Dissolution, Migration, and Deposition of Transition Metal Ions in Li-Ion Batteries Exemplified by Mn-Based Cathodes–a Critical Review. *Energy Environ. Sci.* **2018**, *11* (2), 243–257.

(9) Tang, D.; Sun, Y.; Yang, Z.; Ben, L.; Gu, L.; Huang, X. Surface Structure Evolution of $LiMn_2O_4$ Cathode Material upon Charge/Discharge. *Chem. Mater.* **2014**, *26* (11), 3535–3543.

(10) Zhou, G.; Sun, X.; Li, Q.-H.; Wang, X.; Zhang, J.-N.; Yang, W.; Yu, X.; Xiao, R.; Li, H. Mn Ion

Dissolution Mechanism for Lithium-Ion Battery with LiMn2O4 Cathode: In Situ Ultraviolet–Visible Spectroscopy and Ab Initio Molecular Dynamics Simulations. *J. Phys. Chem. Lett.* **2020**, *11* (8), 3051–3057.

(11) Zhu, X.; Meng, F.; Zhang, Q.; Xue, L.; Zhu, H.; Lan, S.; Liu, Q.; Zhao, J.; Zhuang, Y.; Guo, Q. LiMnO2 Cathode Stabilized by Interfacial Orbital Ordering for Sustainable Lithium-Ion Batteries. *Nat. Sustain.* **2021**, *4* (5), 392–401.

(12) Lin, R.; He, Y.; Wang, C.; Zou, P.; Hu, E.; Yang, X.-Q.; Xu, K.; Xin, H. L. Characterization of the Structure and Chemistry of the Solid–Electrolyte Interface by Cryo-EM Leads to High-Performance Solid-State Li-Metal Batteries. *Nat. Nanotechnol.* **2022**, *17*, 768–776.

(13) Cao, L.; Li, D.; Pollard, T.; Deng, T.; Zhang, B.; Yang, C.; Chen, L.; Vatamanu, J.; Hu, E.; Hourwitz, M. J. Fluorinated Interphase Enables Reversible Aqueous Zinc Battery Chemistries. *Nat. Nanotechnol.* **2021**, *16* (8), 902–910.

(14) Liu, T.; Lin, L.; Bi, X.; Tian, L.; Yang, K.; Liu, J.; Li, M.; Chen, Z.; Lu, J.; Amine, K. In Situ Quantification of Interphasial Chemistry in Li-Ion Battery. *Nat. Nanotechnol.* **2019**, *14* (1), 50–56.

(15) Xiang, Y.; Tao, M.; Zhong, G.; Liang, Z.; Zheng, G.; Huang, X.; Liu, X.; Jin, Y.; Xu, N.; Armand, M. Quantitatively Analyzing the Failure Processes of Rechargeable Li Metal Batteries. *Sci. Adv.* **2021**, *7* (46), eabj3423.

(16) Liu, T.; Dai, A.; Lu, J.; Yuan, Y.; Xiao, Y.; Yu, L.; Li, M.; Gim, J.; Ma, L.; Liu, J. Correlation between Manganese Dissolution and Dynamic Phase Stability in Spinel-Based Lithium-Ion Battery. *Nat. Commun.* **2019**, *10*, 4721.

(17) Xu, C.; Märker, K.; Lee, J.; Mahadevegowda, A.; Reeves, P. J.; Day, S. J.; Groh, M. F.; Emge, S. P.; Ducati, C.; Layla Mehdi, B. Bulk Fatigue Induced by Surface Reconstruction in Layered Ni-Rich Cathodes for Li-Ion Batteries. *Nat. Mater.* **2021**, *20* (1), 84–92.

(18) Lin, F.; Markus, I. M.; Nordlund, D.; Weng, T.-C.; Asta, M. D.; Xin, H. L.; Doeff, M. M. Surface Reconstruction and Chemical Evolution of Stoichiometric Layered Cathode Materials for Lithium-Ion Batteries. *Nat. Commun.* **2014**, *5*, 3529.

(19) Liu, X.; Wang, D.; Liu, G.; Srinivasan, V.; Liu, Z.; Hussain, Z.; Yang, W. Distinct Charge Dynamics in Battery Electrodes Revealed by in Situ and Operando Soft X-Ray Spectroscopy. *Nat. Commun.* **2013**, *4* (1), 2568.

(20) Yuan, Y.; Amine, K.; Lu, J.; Shahbazian-Yassar, R. Understanding Materials Challenges for Rechargeable Ion Batteries with in Situ Transmission Electron Microscopy. *Nat. Commun.* **2017**, *8*, 15806.

(21) Jaumaux, P.; Yang, X.; Zhang, B.; Safaei, J.; Tang, X.; Zhou, D.; Wang, C.; Wang, G. Localized Water-In-Salt Electrolyte for Aqueous Lithium-Ion Batteries. *Angew. Chemie Int. Ed.* **2021**, *60* (36), 19965–19973.

(22) Suo, L.; Borodin, O.; Gao, T.; Olguin, M.; Ho, J.; Fan, X.; Luo, C.; Wang, C.; Xu, K. "Water-in-Salt" Electrolyte Enables High-Voltage Aqueous Lithium-Ion Chemistries. *Science* **2015**, *350* (6263), 938–943.

(23) Xu, J.; Ji, X.; Zhang, J.; Yang, C.; Wang, P.; Liu, S.; Ludwig, K.; Chen, F.; Kofinas, P.; Wang, C. Aqueous Electrolyte Design for Super-Stable 2.5 V $LiMn_2O_4$|| $Li_4Ti_5O_{12}$ Pouch Cells. *Nat. Energy* **2022**, *7* (2), 186–193.

(24) Xie, J.; Liang, Z.; Lu, Y.-C. Molecular Crowding Electrolytes for High-Voltage Aqueous Batteries. *Nat. Mater.* **2020**, *19* (9), 1006–1011.

(25) Wang, C.; Xing, L.; Vatamanu, J.; Chen, Z.; Lan, G.; Li, W.; Xu, K. Overlooked Electrolyte Destabilization by Manganese (II) in Lithium-Ion Batteries. *Nat. Commun.* **2019**, *10*, 3423.

(26) Leifer, N.; Schipper, F.; Erickson, E. M.; Ghanty, C.; Talianker, M.; Grinblat, J.; Julien, C. M.;

Markovsky, B.; Aurbach, D. Studies of Spinel-to-Layered Structural Transformations in LiMn2O4 Electrodes Charged to High Voltages. *J. Phys. Chem. C* **2017**, *121* (17), 9120–9130.

(27) Vissers, D. R.; Chen, Z.; Shao, Y.; Engelhard, M.; Das, U.; Redfern, P.; Curtiss, L. A.; Pan, B.; Liu, J.; Amine, K. Role of Manganese Deposition on Graphite in the Capacity Fading of Lithium Ion Batteries. *ACS Appl. Mater. Interfaces* **2016**, *8* (22), 14244–14251.

(28) Ren, Q.; Yuan, Y.; Wang, S. Interfacial Strategies for Suppression of Mn Dissolution in Rechargeable Battery Cathode Materials. *ACS Appl. Mater. Interfaces* **2021**.

(29) Xu, W.; Zheng, Y.; Cheng, Y.; Qi, R.; Peng, H.; Lin, H.; Huang, R. Understanding the Effect of Al Doping on the Electrochemical Performance Improvement of the $LiMn_2O_4$ Cathode Material. *ACS Appl. Mater. Interfaces* **2021**, *13* (38), 45446–45454.

(30) Lee, S.; Cho, Y.; Song, H.; Lee, K. T.; Cho, J. Carbon-coated Single-crystal $LiMn_2O_4$ Nanoparticle Clusters as Cathode Material for High-energy and High-power Lithium-ion Batteries. *Angew. Chemie* **2012**, *124* (35), 8878–8882.

(31) Wandt, J.; Freiberg, A.; Thomas, R.; Gorlin, Y.; Siebel, A.; Jung, R.; Gasteiger, H. A.; Tromp, M. Transition Metal Dissolution and Deposition in Li-Ion Batteries Investigated by Operando X-Ray Absorption Spectroscopy. *J. Mater. Chem. A* **2016**, *4* (47), 18300–18305.

(32) Gao, X.; Ikuhara, Y. H.; Fisher, C. A. J.; Huang, R.; Kuwabara, A.; Moriwake, H.; Kohama, K.; Ikuhara, Y. Oxygen Loss and Surface Degradation during Electrochemical Cycling of Lithium-Ion Battery Cathode Material $LiMn_2O_4$. *J. Mater. Chem. A* **2019**, *7* (15), 8845–8854.

(33) Santo, K. P.; Neimark, A. V. Effects of Metal-Polymer Complexation on Structure and Transport Properties of Metal-Substituted Polyelectrolyte Membranes. *J. Colloid Interface Sci.* **2021**, *602*, 654–668.

(34) Kumar, R.; Pasupathi, S.; Pollet, B. G.; Scott, K. Nafion-Stabilised Platinum Nanoparticles

Supported on Titanium Nitride: An Efficient and Durable Electrocatalyst for Phosphoric Acid Based Polymer Electrolyte Fuel Cells. *Electrochim. Acta* **2013**, *109*, 365–369.

(35) Kuai, C.; Xu, Z.; Xi, C.; Hu, A.; Yang, Z.; Zhang, Y.; Sun, C.-J.; Li, L.; Sokaras, D.; Dong, C. Phase Segregation Reversibility in Mixed-Metal Hydroxide Water Oxidation Catalysts. *Nat. Catal.* **2020**, *3* (9), 743–753.

(36) Yang, Y.; Xu, R.; Zhang, K.; Lee, S.; Mu, L.; Liu, P.; Waters, C. K.; Spence, S.; Xu, Z.; Wei, C.; et al. Quantification of Heterogeneous Degradation in Li-Ion Batteries. *Adv. Energy Mater.* **2019**, *9* (25), 1900674.

(37) Li, J.; Sharma, N.; Jiang, Z.; Yang, Y.; Monaco, F.; Xu, Z.; Hou, D.; Ratner, D.; Pianetta, P.; Cloetens, P. Dynamics of Particle Network in Composite Battery Cathodes. *Science* **2022**, *376* (6592), 517–521.

(38) Jang, D. H.; Oh, S. M. Electrolyte Effects on Spinel Dissolution and Cathodic Capacity Losses in 4 V $Li/Li_xMn_2O_4$ Rechargeable Cells. *J. Electrochem. Soc.* **1997**, *144* (10), 3342.

(39) Sarapuu, A.; Hussain, S.; Kasikov, A.; Pollet, B. G.; Tammeveski, K. Electroreduction of Oxygen on Nafion®-Coated Thin Platinum Films in Acid Media. *J. Electroanal. Chem.* **2019**, *848*, 113292.

(40) Yang, C.; Han, N.; Wang, Y.; Yuan, X.-Z.; Xu, J.; Huang, H.; Fan, J.; Li, H.; Wang, H. A Novel Approach to Fabricate Membrane Electrode Assembly by Directly Coating the Nafion Ionomer on Catalyst Layers for Proton-Exchange Membrane Fuel Cells. *ACS Sustain. Chem. Eng.* **2020**, *8* (26), 9803–9812.

(41) Sharma, P. P.; Kim, D. A Facile and Sustainable Enhancement of Anti-Oxidation Stability of Nafion Membrane. *Membranes (Basel).* **2022**, *12* (5), 521.

Methods:

Material Preparation:

The active material $LiMn_2O_4$ (LMO) was provided by the U.S. Department of Energy's (DOE) CAMP Facility (Cell Analysis, Modeling and Prototyping) at Argonne National Laboratory. The Lithium bis(trifluoromethanesulfonyl)imide (LiTFSI) salts (99.95%), Nafion solution (5wt. %, contains 45% water) and Mn_3O_4 (97%) were purchased from Sigma Aldrich. MnO_2 (activated, tech. 90%) was purchased from Alfa Aesar. MnO_2 was heated at 350°C for 12 hours before using.

Electrochemical Measurements:

In the three-electrode system, Ag/AgCl (3M NaCl) (MF-2052, BASi Research) and Pt wire (Sigma Aldrich) were utilized as reference and counter electrodes, respectively. The electrolyte was prepared by dissolving 2 M LiTFSI in the DI water. The $LiMn_2O_4$ (LMO) slurry was prepared by mixing active materials, carbon black (CB) and polyvinylidene fluoride (PVDF) with a ratio of 8:1:1 and then drop-casted onto carbon paper. The active mass loading was estimated to be ~3 mg/cm^2. The composition (% weight) of LMO electrodes used for the particle-level analysis is 6:3:1 (LMO: PVDF: CB) to stabilize the particle during XFM experiments. The mass loading is ~2 mg/cm^2. For the Nafion-added LMO electrodes, 45 µL Nafion solution was added to the LMO slurry containing 300 mg of the solid mixture. Then the slurry was drop-casted on the carbon paper with a mass loading of ~3.5 mg/cm^2. The composition (% weight) of drop-casted Mn_3O_4 and MnO_2 electrodes was 8:1:1 (Active Material: PVDF: CB), and the mass loading was ~4 mg/cm^2. The cyclic voltammetry (CV) measurement was conducted at a scan rate of 5 mV/s within -0.1 – 1.5 V (vs. Ag/AgCl). The galvanostatic cycling with potential limitation (GCPL, normal charging-discharging process) measurement was conducted within 0 – 1.2 V (vs. Ag/AgCl) and the current density was 100 mA/g. The Chronoamperometry (CA) was conducted at different voltages (-0.1 V, 0.9 V, 1.2 V) for the measurements. For all electrochemical measurements were conducted using a Potentiostat (SP-150, BioLogic, France).

SEM and XRD characterization:

The morphology of the materials was characterized on a LEO 1550 field-emission scanning electron microscopy (SEM) with an accelerating voltage of 6 kV. EDS measurements were carried out with the SEM with an accelerating voltage of 20 kV. The EDS sample of soaked Nafion membrane is washed with DI water three times and dried at 80°C to remove the residual water. The lab X-ray diffraction (XRD) results were obtained on a Rigaku Miniflex II diffractometer with a Cu Kα X-ray radiation (λ = 1.54 Å) in a scan range of 10-70°.

In situ XFM Measurement:

The *in situ* XFM was performed at the 2-ID-E beamline of Advanced Photon Source, Argonne National Laboratory. The *in situ* cell design can be found in previous report[35]. The samples were prepared by the same drop-casting method as described above. The Ag/AgCl and carbon rod serve as the reference and counter electrodes, respectively, during the electrochemical measurements. The bulk electrodes were raster scanned by a sub-micrometer (~700 nm) focused 10.5 KeV X-ray beam with a step size of 2 μm for electrode-scale measurements and 300 nm for particle-level measurements along x and y axes, except for the step size of XFM measurement in Figure 5c, which is 2 μm along x and y axes. During the measurement, the samples were aligned at an angle of ~60° with respect to the incident beam. The fluorescent X-ray signals were detected with a four-element silicon-drift Vortex detector and the raw data were processed and quantified with XRF MAPS software developed by Argonne National Lab .

In situ Hard XAS Measurement:

Hard XAS measurements were conducted at beamline 4-1 at the Stanford Synchrotron Radiation Lightsource, SLAC National Accelerator Laboratory. The sample preparation and cell configuration were the same as in the XFM measurements. The Mn K-edge spectra was collected in the fluorescence mode, with samples aligned at an angle of ~45° with respect to the incident beam and fluorescent detector. The Mn metal foil was used to calibrate the edge energy. All XANES and EXAFS spectra were analyzed with

the Athena software. The fitting of EXAFS results was analyzed with Artemis software. The current density was 20 mA/g for the charging-discharging process during *in situ* XAS measurements.

TEM measurement:

High Annular Dark Field -Scanning Transmission Electron Microscope (HAADF-STEM) and Electron Energy loss Spectroscopy (EELS) measurements were performed with Thermo-Fisher Talos F200X and Hitachi HD2700C at an accelerating voltage of 200 kV at the Center for Functional Nanomaterials, Brookhaven National Laboratory. The background subtraction of EELS spectra was processed with the digital micrograph (Gatan) software.

Soft XAS Measurement:

Soft XAS was performed at the Stanford Synchrotron Radiation Lightsource (SSRL), beamline 10-1, SLAC National Accelerator Laboratory using a ring current of 350 mA and a 1000 L mm^{-1} spherical grating monochromator with 20 μm entrance and exit slits, providing ≈10^{11} ph s^{-1} at 0.2 eV resolution in a 1 mm^2 beam spot. Data were acquired under ultrahigh vacuum (10^{-9} Torr) in a single load at room temperature using TEY, where the sample drain current was collected. The samples were mounted on an aluminum sample holder in an Ar-filled glove box and well-sealed for transfer.

Data Availability:

The data that support the findings of this study are available within the paper and its Supplementary Information. Any other data are available from the corresponding author on request.

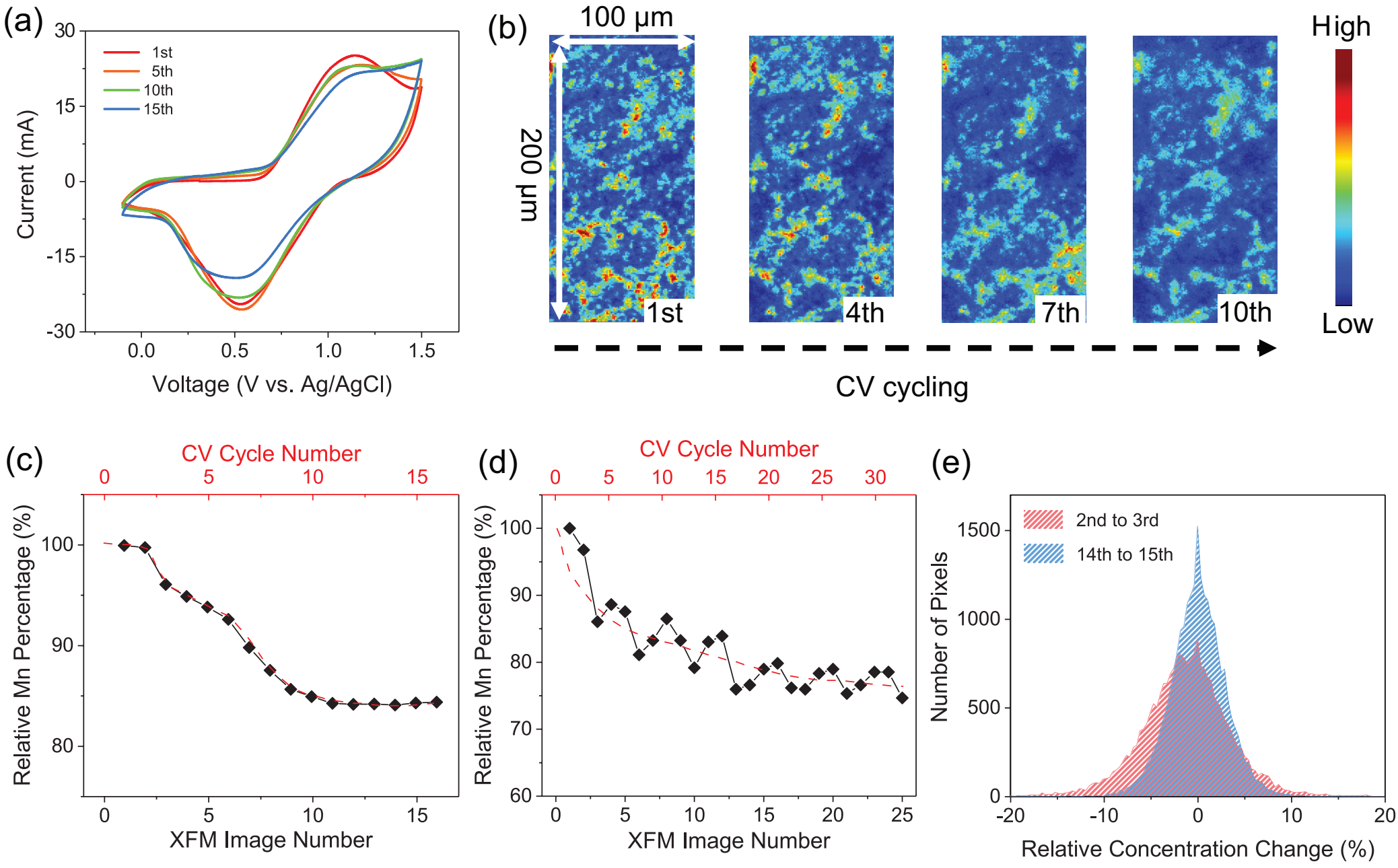
(a)
1st
5th
10th
15th
Current (mA)
Voltage (V vs. Ag/AgCl)
(b)
100 μm
200 μm
1st
4th
7th
10th
High
Low
CV cycling
(c)
CV Cycle Number
Relative Mn Percentage (%)
XFM Image Number
(d)
CV Cycle Number
Relative Mn Percentage (%)
XFM Image Number
(e)
2nd to 3rd
14th to 15th
Number of Pixels
Relative Concentration Change (%)

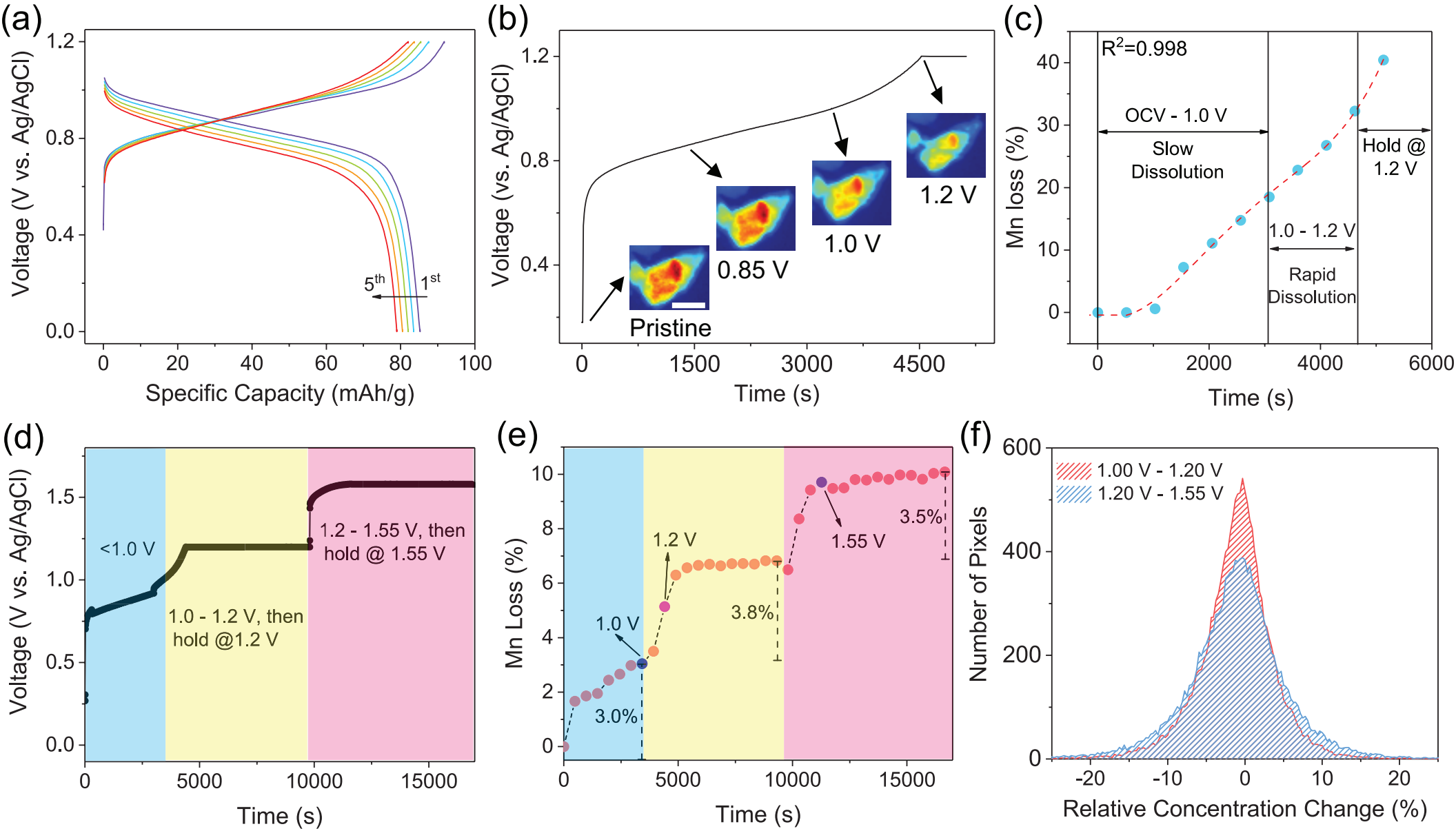
(a)
Voltage (V vs. Ag/AgCl)
Specific Capacity (mAh/g)
5th
1st
(b)
Voltage (vs. Ag/AgCl)
Time (s)
Pristine
0.85 V
1.0 V
1.2 V
(c)
R2=0.998
OCV - 1.0 V
Slow Dissolution
1.0 - 1.2 V
Rapid Dissolution
Hold @ 1.2 V
Mn loss (%)
Time (s)
(d)
Voltage (V vs. Ag/AgCl)
<1.0 V
1.0 - 1.2 V, then hold @1.2 V
1.2 - 1.55 V, then hold @ 1.55 V
Time (s)
(e)
Mn Loss (%)
1.0 V
1.2 V
1.55 V
3.0%
3.8%
3.5%
Time (s)
(f)
1.00 V - 1.20 V
1.20 V - 1.55 V
Number of Pixels
Relative Concentration Change (%)

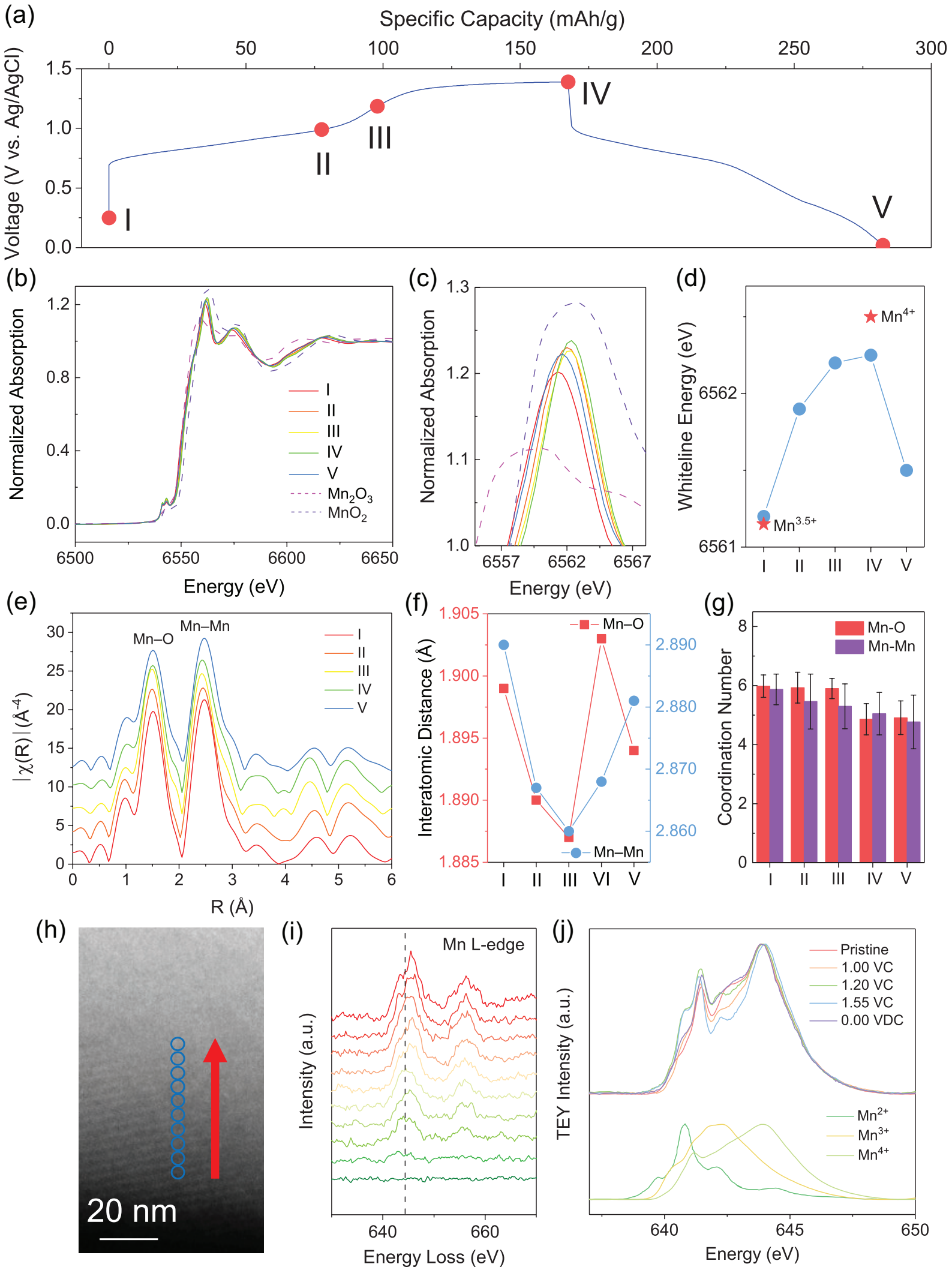
(a)
Specific Capacity (mAh/g)
Voltage (V vs. Ag/AgCl)
I
II
III
IV
V
(b)
Normalized Absorption
Energy (eV)
Mn2O3
MnO2
(c)
Normalized Absorption
Energy (eV)
(d)
Whiteline Energy (eV)
Mn4+
Mn3.5+
(e)
Mn–O
Mn–Mn
R (Å)
(f)
Interatomic Distance (Å)
Mn–O
Mn–Mn
(g)
Coordination Number
Mn-O
Mn-Mn
(h)
20 nm
(i)
Mn L-edge
Intensity (a.u.)
Energy Loss (eV)
(j)
TEY Intensity (a.u.)
Pristine
1.00 VC
1.20 VC
1.55 VC
0.00 VDC
Mn2+
Mn3+
Mn4+
Energy (eV)

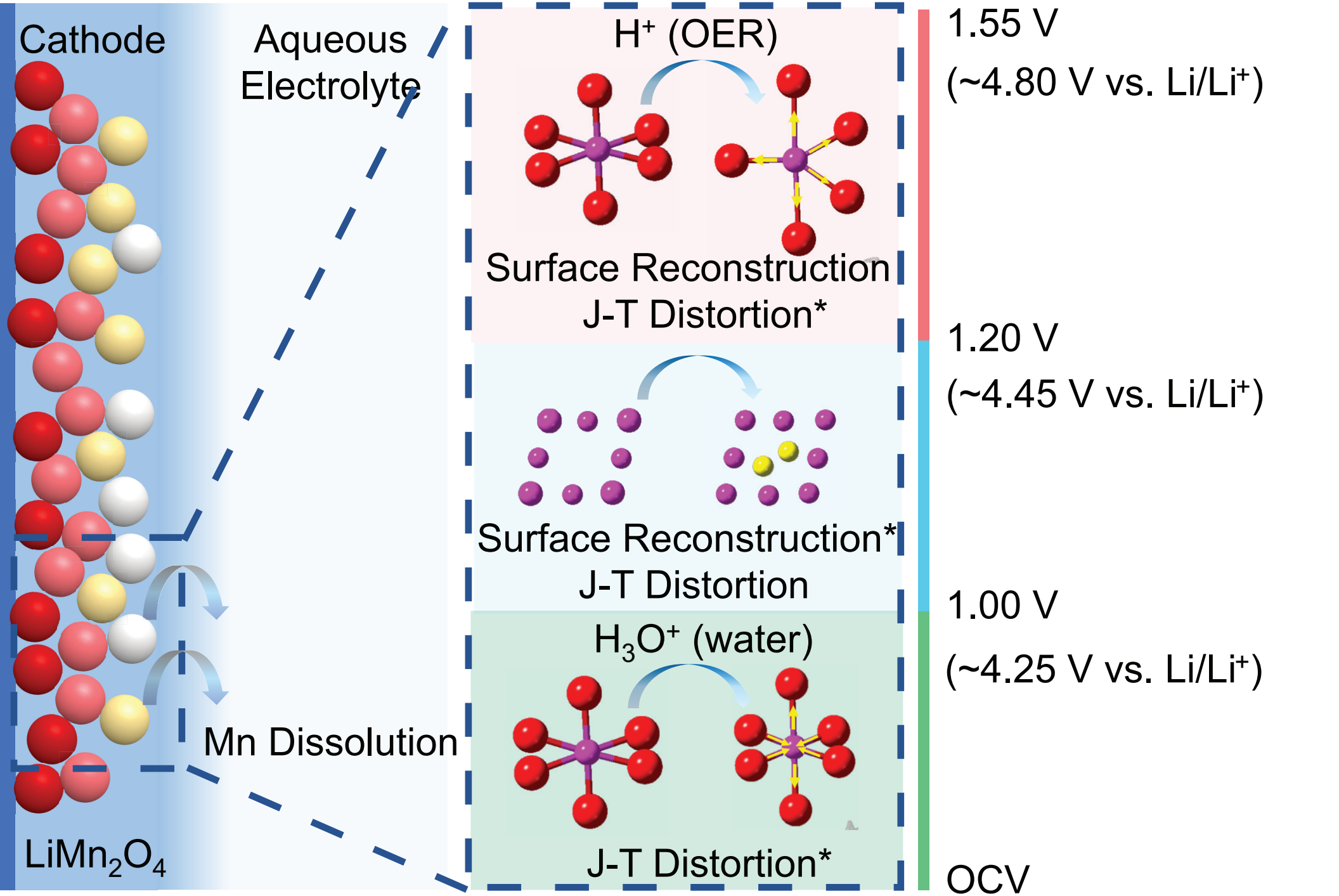
Cathode
Aqueous Electrolyte
$LiMn_2O_4$
Mn Dissolution
H^+ (OER)
Surface Reconstruction
J-T Distortion*
Surface Reconstruction*
J-T Distortion
H_3O^+ (water)
J-T Distortion*
1.55 V
(~4.80 V vs. Li/Li$^+$)
1.20 V
(~4.45 V vs. Li/Li$^+$)
1.00 V
(~4.25 V vs. Li/Li$^+$)
OCV

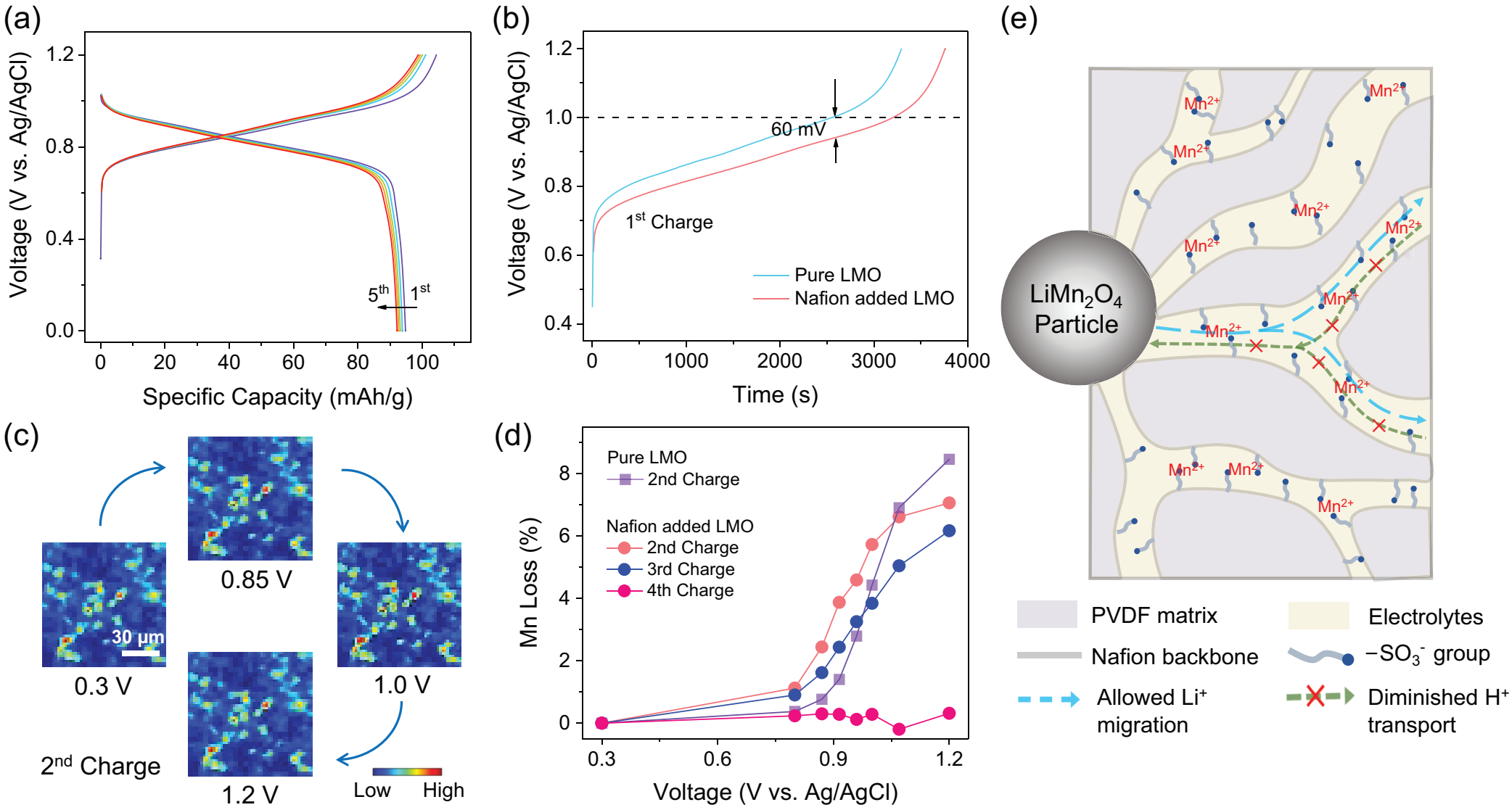
(a)
Voltage (V vs. Ag/AgCl)
Specific Capacity (mAh/g)
5th
1st
(b)
Voltage (V vs. Ag/AgCl)
Time (s)
60 mV
1st Charge
Pure LMO
Nafion added LMO
(c)
0.3 V
0.85 V
1.0 V
1.2 V
2nd Charge
30 μm
Low
High
(d)
Mn Loss (%)
Voltage (V vs. Ag/AgCl)
Pure LMO
2nd Charge
Nafion added LMO
2nd Charge
3rd Charge
4th Charge
(e)
LiMn2O4 Particle
Mn2+
PVDF matrix
Electrolytes
Nafion backbone
−SO3- group
Allowed Li+ migration
Diminished H+ transport